J. Fluid Mech. (2024), *vol*. 997, A72, doi:10.1017/jfm.2024.852

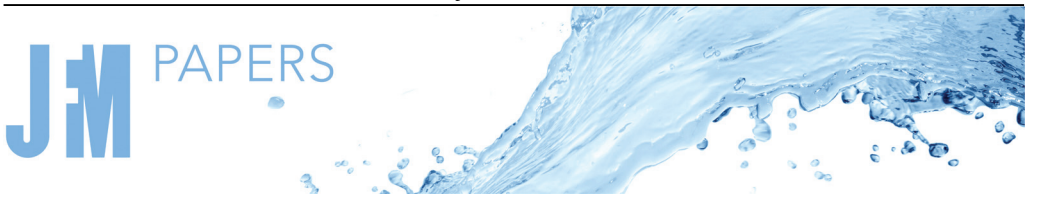

Effects of asymmetric rough boundaries on turbulent Rayleigh–Bénard convection

Bu-Ying-Chao Cheng[1],‡, **Lu Zhang**[2],†,‡, **Ke-Qing Xia**[2],† **and Yi-Chao Xie**[3],†

[1]Department of Physics, The Chinese University of Hong Kong, Shatin, Hong Kong, PR China

[2]Center for Complex Flows and Soft Matter Research and Department of Mechanics and Aerospace Engineering, Southern University of Science and Technology, Shenzhen 518055, PR China

[3]State Key Laboratory for Strength and Vibration of Mechanical Structures and School of Aerospace, Xi'an Jiaotong University, Xi'an 710049, PR China

(Received 9 April 2024; revised 26 July 2024; accepted 1 September 2024)

We report on an experimental study of turbulent Rayleigh–Bénard convection with asymmetric top and bottom plates. The plates are covered with pyramid-shaped roughness elements whose aspect ratios are $\lambda = 1$ or $\lambda = 4$. In the low-Rayleigh-number regime ($Ra < 1.9 \times 10^9$), the heat transport efficiencies in the asymmetric cells, characterized by the Nusselt number, are smaller than those measured in a symmetric $\lambda = 1$ cell and are greater than those for a symmetric $\lambda = 4$ cell, whereas in the high-Rayleigh-number regime ($Ra > 1.9 \times 10^9$), the Nusselt numbers of the asymmetric cells are, in turn, greater than those for the symmetric cell with $\lambda = 1$ and smaller than those for the symmetric cell with $\lambda = 4$. In addition, the heat transports of individual plates are studied based on the temperature drops across both halves of the cell. In the low-Ra regime, the $\lambda = 1$ plate shows higher heat transfer than the $\lambda = 4$ plate, while for the high-Ra regime, the $\lambda = 4$ plate shows a higher heat transport ability. In both regimes, the individual Nusselt number of the plate with lower heat transfer is insensitive to the topology of the other plate. Besides, it is found that the symmetry of the centre temperature distribution is robust to the symmetry breaking of boundary topographies. For the Ra range explored, a weak temperature inversion is observed in the bulk of asymmetric rough cells. Finally, we remark that the temperature fluctuation at the cell centre and the Reynolds number associated with the large-scale circulation show universal power laws in terms of the flux Rayleigh number as $\sigma_{T_c} \sim Ra_F^{0.68}$ and $Re_{LSC} \sim Ra_F^{0.36}$, respectively.

Key words: Bénard convection, turbulent convection

† Email addresses for correspondence: zhangl39@sustech.edu.cn, xiakq@sustech.edu.cn, yichao.xie@xjtu.edu.cn

‡ B.-Y.-C.C. & L.Z. contributed equally to this work.

1. Introduction

Symmetry is a crucial concept in physics, mathematics and even the arts. For a dynamical system, symmetry breaking is often associated with violation of a conservation law and global state bifurcation. Being a classic dynamical system, turbulent Rayleigh–Bénard convection (RBC) is, by its definition, highly symmetric and a well-known paradigm for studying thermal-driven turbulence. It involves a fluid layer strongly heated from below and cooled from above. Under the Oberbeck–Boussinesq (OB) approximation (Oberbeck 1879; Boussinesq 1903), the governing equations of RBC satisfy translation, reflection and rotational symmetry (Zhang, Ding & Xia 2021). The RBC system generally has two control parameters, i.e. the Rayleigh number $Ra = \alpha g \Delta T H^3/(\nu\kappa)$ and the Prandtl number $Pr = \nu/\kappa$. Here, g is the gravitational acceleration constant, and α, ν and κ are the isobaric thermal expansion coefficient, the kinematic viscosity and the thermal diffusivity of the convecting fluid, respectively, while ΔT and H are the temperature difference across the fluid layer and the height of the convection domain. In practice, one needs a third parameter, i.e. the aspect ratio $\Gamma = D/H$, to describe the finite horizontal scale of the domain. For a cylindrical cell, which is the case of the present study, D is just the diameter.

In an RBC cell with an aspect ratio around unity, when the flow is fully turbulent for large enough Ra, a coherent structure, known as the large-scale circulation (LSC), spans almost the entire convection domain (Krishnamurti & Howard 1981; Xi, Lam & Xia 2004; Ren *et al.* 2022). The LSC is a quasi-two-dimensional structure that rotates in a vertical plane just like a 'flywheel'. The formation of the LSC can be considered as a classic example of spontaneous symmetry breaking in turbulence. In the long term, the LSC can sample all azimuthal locations by reorientation (Brown, Nikolaenko & Ahlers 2005; Sun, Xia & Tong 2005), resulting in dynamical restoration of the azimuthal symmetry. The LSC is also rich in other dynamical behaviours, including torsion, sloshing, azimuthal meandering, cessation and reversal (Xi & Xia 2007; Xi *et al.* 2009; Zhou *et al.* 2009; Xie, Wei & Xia 2013), the last of which can also be interpreted as a process that restores the statistical symmetry of the system (Huang *et al.* 2015).

The up–down reflection symmetry of RBC can be broken for many reasons, for example, adopting different temperature/velocity boundary conditions on the top and bottom, or violating the OB approximation. The latter is also known as the non-Oberbeck–Boussinesq (NOB) effect (Ahlers *et al.* 2006). The NOB effect sets in when the temperature difference across the top and bottom plates, ΔT, is too large so that material properties of the working fluid can no longer be treated as temperature-independent. Previous studies showed that the Nusselt number and Reynolds number (which quantify the non-dimensionalized heat-transfer efficiency and flow strength, respectively) for the OB and NOB cases only show slight differences (Ahlers *et al.* 2006, 2007; Demou & Grigoriadis 2019; Wan *et al.* 2020). In addition, the Nusselt number is also found to be insensitive to the symmetry property of the temperature boundary conditions (Verzicco & Sreenivasan 2008; Johnston & Doering 2009; Stevens, Lohse & Verzicco 2011; Urban *et al.* 2021), even though both the flow strength and the flow structure exhibit remarkable changes for different combinations of constant temperature and constant flux boundary conditions (Huang *et al.* 2015; Vieweg, Scheel & Schumacher 2021). On the other hand, top–bottom asymmetry induced by slip–non-slip velocity boundary conditions not only alters the flow structure but also causes observable changes in the heat transport (Xie & Xia 2013; van der Poel *et al.* 2014; Huang *et al.* 2022).

It is known that the presence of a rough surface has a significant impact on the transport properties in RBC (Shen, Tong & Xia 1996; Qiu, Xia & Tong 2005; Xie & Xia 2017). As one might expect, the up–down reflection symmetry of RBC can also be violated by

applying different roughness on the top and bottom boundaries (Tisserand *et al.* 2011; Salort *et al.* 2014; Wei *et al.* 2014; Liot *et al.* 2016, 2017; Rusaouën *et al.* 2018; Jiang *et al.* 2018; Belkadi *et al.* 2020, 2021). Tisserand *et al.* (2011) conducted heat transport measurements in a RBC cell with a smooth top plate and a rough bottom plate. They found that the individual *Nu–Ra* relation of the smooth top plate was approximately the same as that measured in a symmetric smooth cell. They also concluded that the heat transport behaviours of the smooth and rough plates are independent, and the interaction between the flow and solid boundary is mainly a local process. Later, researchers from the same group (Rusaouën *et al.* 2018) carried out heat-transfer measurements in asymmetric cells with larger roughness elements and different aspect ratios, and they confirmed the three heat transport regimes in symmetric rough cells reported by Xie & Xia (2017). Wei *et al.* (2014) conducted a systematic study of smooth–rough boundary asymmetry in turbulent RBC. Their results showed that the heat transport property of a smooth plate is robust to the changes in geometries and temperature boundary conditions of the opposite plate. In contrast, a rough plate is susceptible to the topology (smooth or rough) and the temperature boundary condition of the other plate. By conducting direct numerical simulations, Belkadi *et al.* (2021) confirmed the findings above and highlighted the role of roughness valleys in determining global heat transport. Using particle image velocimetry (PIV), Liot *et al.* (2016) measured the boundary layer structure at the rough plate of a smooth–rough asymmetric RBC cell using air as the working fluid. They found that at low Rayleigh number, there is no heat-transfer enhancement and the velocity profiles are compatible with those measured in a smooth cell, while at high Rayleigh number, heat transfer enhancement is observed and the velocity profiles are closer to the logarithmic profiles expected in the case of turbulent boundary layers. Later, researchers from the same group (Liot *et al.* 2017) conducted PIV measurements in a smooth–rough asymmetric cell and a smooth–smooth (SS) symmetric cell, both using water as the working fluid. With the presence of roughness elements, they found a significant increase in the velocity fluctuations but only a subtle change in the mean flow strength. In addition, the smooth–rough cell also featured a breaking of the top–bottom symmetry in its vertical velocity profile.

To our knowledge, almost all existing studies on asymmetric boundary geometries were carried out using a smooth plate and a rough plate. In fact, the up–down symmetry can be broken for any combination of plates with different geometries. It is still unclear how geometrical asymmetry, in general, affects the transport property and how different boundary geometries interact with each other through the bulk flow. In the present study, we use plates with different pyramid-shaped roughness elements to explore how turbulent thermal convection responds to a geometrical boundary asymmetry. For many industrial applications, heating and cooling usually take place at different scales, and employing different kinds of roughness elements (pin-fins) is a common solution for efficient thermal dissipation (Ahmed *et al.* 2018; He, Yan & Zhang 2021). But the general questions of how heating and cooling sites with different (asymmetric) roughnesses interact in thermally driven turbulence and which kind of roughness controls the heat transport both remain open, which also motivates the present study.

Systematic measurements of the heat transport, the mean temperature profile, the temperature fluctuations and the flow strength were carried out. We will also compare the results obtained in the present study with those measured in symmetric rough cells reported by Xie & Xia (2017) whenever possible. The rest of the paper is organized as follows. In § 2, we introduce the apparatus used in this study. The experimental results are then presented in § 3. This section is further divided into six subsections, in which we will discuss the global heat transport, the centre temperature behaviour, the heat transport

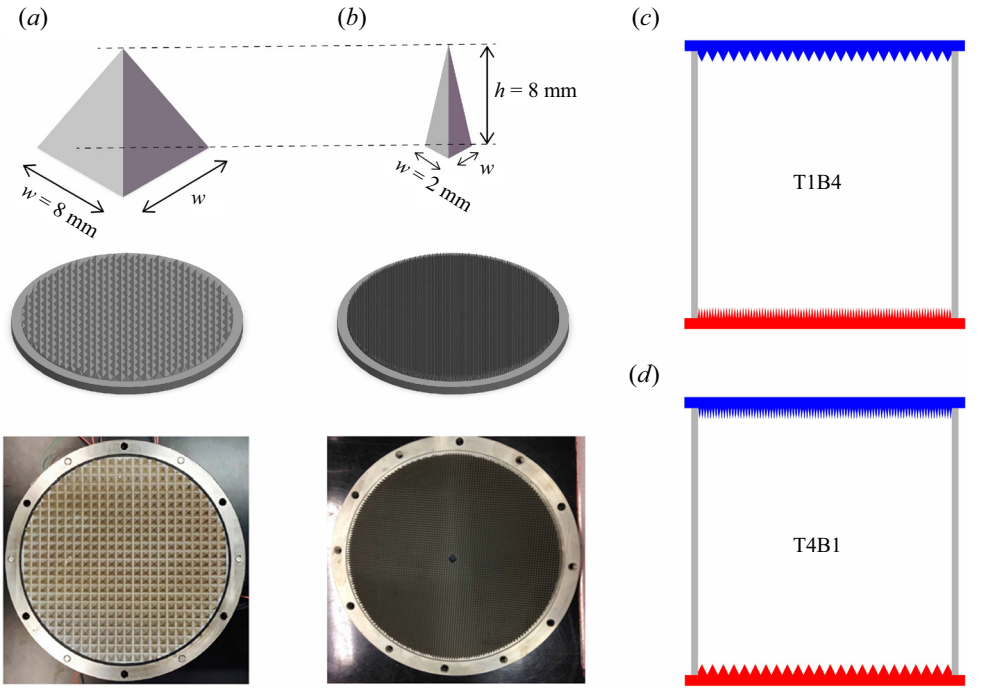

Figure 1. Panels (*a*,*b*) show photographs of the rough plates used in this study with $\lambda = 1$ and $\lambda = 4$, respectively. Panels (*c*,*d*) show schematics of the asymmetric Rayleigh–Bénard (RB) cells, with red representing the heating plates and blue the cooling plates.

properties of individual plates, the bulk temperature inversion, the Reynolds number and the convective temperature and velocity scales in turn. Finally, we summarize our main findings in § 4.

2. Experimental set-up

Geometric boundary asymmetry is introduced using plates with two types of pyramid-like roughness elements (see figure 1*a*,*b*). The height of the roughness element is fixed at $h = 8$ mm, and the base width is $w = 2$ mm or 8 mm. So the corresponding aspect ratio of the roughness elements, defined as $\lambda = h/w$, is either 1 or 4. In the experiments, one cell is assembled with a $\lambda = 1$ top plate and a $\lambda = 4$ bottom plate, which we refer to as the 'T1B4' set (figure 1*c*) hereinafter. The other cell is assembled by switching the top and bottom plates, and we refer to this set as 'T4B1' (figure 1*d*).

The convection cells are both cylindrical in shape, with diameters and heights being $D = 192$ and $H = 193$ mm, respectively, so their aspect ratios are close to unity. The sidewalls of both cells are made of 4 mm thickness Plexiglas. The top plate is cooled by passing temperature-regulated water through a chamber fitted on its top surface. The temperature stability of the cooling water is better than 0.005 K. The bottom plate was embedded with resistive heaters. The heaters are connected to a DC power supply with a voltage stability of approximately 99.99 % for bottom heating. With the above settings, the thermal boundary conditions are constant temperature at the top plate and constant heat flux at the bottom plate. The temperature of the top/bottom plate is measured using four/five thermistors. The distance between the thermistor head and the valley of the roughness elements is approximately 5 mm. In addition, a small waterproof thermistor with a head diameter of 0.38 mm and a response time of approximately 30 ms is used

to measure the temperature at the centre of the cell, T_c. Deionized and degassed water is used as the working fluid throughout the experiments. The centre temperature T_c is kept at 40 °C, corresponding to a Prandtl number of $Pr = 4.34$. In the present study, the Rayleigh number covers a range of $2.6 \times 10^8 \leq Ra \leq 9.8 \times 10^9$. For the temperature profile measurement, another waterproof thermistor is mounted on a linear stepping motor by a stainless-steel tube, which can then move along the vertical centre line of the cell with an accuracy of approximately 4 μm.

For high-precision heat-transfer measurements, the system must have good thermal insulation from the environment. To achieve this, the convection cell is placed inside a homemade copper thermal shield during the measurement. The temperature of the shield was regulated to match T_c with a stability better than 0.1 K. In addition, a copper basin is placed underneath the convection cell to compensate for the downward heat leakage from the bottom plate. A proportional-integral-derivative temperature controller is used to regulate the temperature of the basin by setting its temperature to be the same as that of the bottom plate. The experimental results are listed in table 1.

3. Results and discussions

3.1. *Global heat transport*

Figure 2(*a*) shows the *Nu–Ra* data measured in two sets of asymmetric cells (T1B4 and T4B1). Data taken from the literature for symmetric rough cells (T1B1 and T4B4) (Xie & Xia 2017) and an SS cell (Wei *et al.* 2014) are also plotted as references. For the Rayleigh number range explored, the heat transport efficiencies of symmetric and asymmetric rough cells are considerably higher than in the smooth case. For a clearer view of the differences between the symmetric and asymmetric cells, we present the corresponding compensated plots of $NuRa^{-0.5}$ versus Ra in figure 2(*b*). It is seen that the Nusselt numbers of the two asymmetric sets are just in between the curves for the symmetric rough cells (T1B1 and T4B4), and the four curves cross over at a Rayleigh number of approximately $Ra_c = 1.9 \times 10^9$. This implies that at this particular Rayleigh number Ra_c, the heat transport ability (or equivalently the thermal impedance) of a $\lambda = 1$ rough plate is the same as that of a $\lambda = 4$ rough plate, regardless of whether they are located at the top or bottom of the cell and whether they are assembled symmetrically or asymmetrically. Whereas for $Ra < Ra_c$, the heat transport in asymmetric cells is dominated by the $\lambda = 1$ rough plate and bottlenecked by the $\lambda = 4$ rough plate, for $Ra > Ra_c$ it is the $\lambda = 4$ plate that prompts the heat transfer, and the overall transport is limited by the $\lambda = 1$ plate. It is also worth noting that the *Nu–Ra* relations measured in the two asymmetric cells (T1B4 and T4B1) show the same behaviour, and they differ only by a factor of approximately 5 % at small Rayleigh numbers. This observation also agrees with the fact that the heat-transfer efficiency in thermal convection is insensitive to the applied temperature boundary conditions (Johnston & Doering 2009; Stevens *et al.* 2011; Wei *et al.* 2014). The solid and dashed lines in figure 2(*b*) show effective power-law fits with $Nu = BRa^{\beta}$ to the data before and after the intersection point, respectively. The fitting results are summarized in table 2. As expected, the effective scaling exponents β of the rough cells are all larger than the value of 0.30 for the smooth case. With each data set, the scaling exponents for $Ra \leq 1.9 \times 10^9$ are larger than those for $Ra > 1.9 \times 10^9$. Xie & Xia (2017) interpreted such a transition as a process in which the viscous boundary layer thickness gets thinner than the height of the roughness elements. We emphasize that the present data for asymmetric rough cells are consistent with this physical picture. Lastly, the fact that the *Nu–Ra* curves for asymmetric cells are just in between those measured in the

Cell	No.	ΔT (K)	$T_c - T_m$ (K)	σ_{T_c} (K)	Ra ($\times 10^8$)	Ra_F ($\times 10^{10}$)	Nu	Re ($\times 10^3$)
T4B1	1	6.47	−0.091	0.082	20.5	34.0	165.4	4.52
T4B1	2	6.48	−0.065	0.084	20.6	34.0	165.0	4.36
T4B1	3	8.57	−0.166	0.108	27.2	51.2	188.5	5.01
T4B1	4	12.01	−0.321	0.154	37.8	82.9	219.1	6.18
T4B1	5	15.37	−0.481	0.188	48.2	117	243.6	6.99
T4B1	6	4.75	−0.025	0.061	15.0	21.2	141.0	3.82
T4B1	7	3.09	0.021	0.037	9.81	11.1	112.7	3.11
T4B1	8	1.89	0.032	0.022	5.98	5.12	85.6	2.32
T4B1	9	1.58	0.030	0.019	5.05	3.91	77.3	2.07
T4B1	10	1.14	0.017	0.013	3.64	2.36	64.8	1.69
T4B1	11	1.01	0.012	0.012	3.21	1.93	60.2	1.63
T4B1	12	0.73	−0.007	0.008	2.33	1.20	51.6	1.35
T4B1	13	0.84	0.000	0.009	2.67	1.47	55.0	1.47
T4B1	14	2.17	0.041	0.026	6.92	6.35	91.8	2.45
T4B1	15	1.37	0.030	0.015	4.34	3.06	70.6	1.95
T4B1	16	2.58	0.039	0.031	8.17	8.28	101.4	2.73
T4B1	17	3.79	0.020	0.046	12.1	15.1	124.5	3.39
T4B1	18	10.54	−0.237	0.133	33.3	67.9	204.0	5.71
T4B1	19	29.87	−0.950	0.348	94.7	293	309.4	9.31
T4B1	20	24.65	−0.782	0.290	78.0	224	287.6	8.55
T4B1	21	18.85	−0.573	0.225	59.7	154	258.5	7.53
T4B1	22	15.60	−0.391	0.192	49.4	119	239.8	6.80
T1B4	1	5.39	0.027	0.070	17.0	25.4	148.8	4.32
T1B4	2	1.32	−0.013	0.015	4.14	2.96	71.5	1.91
T1B4	3	19.48	1.115	0.246	62.1	163	262.3	8.28
T1B4	4	11.06	0.366	0.136	35.1	73.6	209.8	6.30
T1B4	5	3.83	−0.019	0.046	12.0	15.1	125.9	3.61
T1B4	6	2.46	−0.047	0.030	7.74	7.77	100.4	2.78
T1B4	7	0.95	0.000	0.011	2.98	1.79	60.1	1.61
T1B4	8	1.79	−0.038	0.020	5.61	4.75	84.6	2.28
T1B4	9	3.09	−0.047	0.038	9.72	10.9	112.7	3.20
T1B4	10	6.67	0.063	0.086	21.1	34.7	164.5	4.86
T1B4	11	8.05	0.133	0.107	25.5	45.7	179.5	5.35
T1B4	12	9.63	0.224	0.125	30.5	59.5	194.9	5.82
T1B4	13	13.96	0.567	0.180	44.4	102	230.3	7.04
T1B4	14	16.62	0.808	0.214	53.0	132	248.1	7.69
T1B4	15	12.80	0.463	0.159	40.7	89.9	221.0	6.72
T1B4	16	6.07	0.021	0.078	19.1	30.1	157.1	4.57
T1B4	17	4.48	−0.046	0.059	14.1	19.2	136.4	3.93
T1B4	18	3.43	−0.032	0.043	10.8	12.9	119.3	3.34
T1B4	19	2.78	−0.041	0.033	8.72	9.31	106.7	2.98
T1B4	20	2.10	−0.057	0.025	6.61	6.11	92.5	2.55
T1B4	21	1.54	−0.036	0.018	4.83	3.75	77.7	2.12
T1B4	22	1.14	−0.022	0.014	3.56	2.35	65.9	1.74
T1B4	23	0.83	−0.005	0.009	2.59	1.45	56.0	1.51
T1B4	24	28.35	2.139	0.345	90.8	278	306.6	10.3
T1B4	25	23.64	1.549	0.308	75.5	215	285.0	9.28
T1B4	26	21.70	1.320	0.269	69.4	193	277.8	8.99
T1B4	27	25.93	1.848	0.317	82.9	244	294.8	9.77
T1B4	28	11.16	0.270	0.147	35.4	73.8	208.4	6.38

Table 1. The temperature difference between the top and bottom plates (ΔT), the difference between the centre temperature and the arithmetic mean temperature of the conducting plates ($T_c - T_m$), the standard deviation of the centre temperature fluctuation (σ_{T_c}), the Rayleigh number (Ra), the flux Rayleigh number (Ra_F), the Nusselt number (Nu) and the Reynolds number (Re). The data sets are listed chronologically.

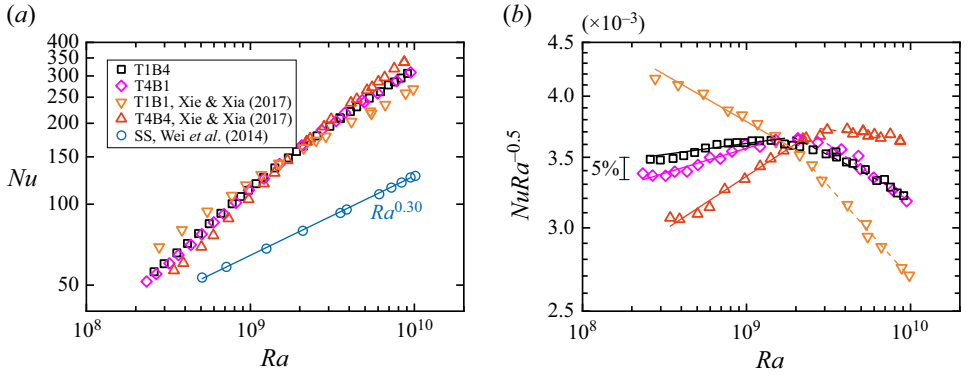

Figure 2. (*a*) The *Nu*–*Ra* relations measured in the T1B4 cell (squares) and the T4B1 cell (diamonds). For comparison, data from the literature for symmetric rough cells (T1B1 and T4B4) and a symmetric smooth cell (SS) are plotted as triangles and circles, respectively. The solid line shows a power-law fit of $Ra^{0.30}$. (*b*) Compensated plots of $NuRa^{-0.5}$. The legends are the same as those in panel (*a*). The solid and dashed lines represent power-law fits to the data in two Rayleigh number regimes. The fitting results are listed in table 2.

	$Ra \leq 1.9 \times 10^9$				$Ra > 1.9 \times 10^9$				
Cell	B	β	C	γ	B	β	C	γ	Data source
T1B4	0.0023	0.52	0.0018	0.09	0.020	0.42	0.055	−0.07	Present study
T4B1	0.0013	0.55	0.0029	0.07	0.039	0.39	0.053	−0.07	Present study
T1B1	0.015	0.43	0.032	−0.05	0.10	0.35	0.33	−0.15	Xie & Xia (2017)
T4B4	0.00052	0.59	0.00091	0.12	0.0040	0.50	0.11	−0.10	Xie & Xia (2017)
SS	0.141	0.30	0.060	−0.10	0.141	0.30	0.060	−0.10	Wei *et al.* (2014)

Table 2. Fitting parameters of $Nu = BRa^{\beta}$ and $\sigma_{T_c}/\Delta T = CRa^{\gamma}$ for different cells.

symmetric cases suggests that using cells with different roughnesses might be an efficient way to extend the Rayleigh number range with high heat-transfer efficiency (Zhu *et al.* 2019; Toppaladoddi *et al.* 2021).

3.2. *Temperature at the cell centre*

Figure 3(*a*) shows the difference between the time-averaged centre temperature T_c and the arithmetic mean temperature of the top and bottom plates, $T_m = (T_t + T_b)/2$, as a function of the temperature difference ΔT applied across the two conducting plates. Here T_t and T_b denote the time-averaged temperatures of the top and bottom plates, respectively. The same quantity measured in a symmetric smooth cell is plotted for reference as well (Ahlers *et al.* 2006). It is seen that for $\Delta T \geq 5$ K (corresponding to $Ra > Ra_c$), the measured centre temperatures T_c show apparent deviations from T_m for all three data sets. For an SS cell, it is known that such deviation results from the NOB effect (Ahlers *et al.* 2006). In this regime, we note that the curve of T1B4 is always higher than in the SS case, which suggests that for the T1B4 cell, the heat-transfer capability of the bottom plate ($\lambda = 4$) is greater than that of the top plate ($\lambda = 1$). In other words, the thermal impedance of the bottom plate is lower than that of the top plate in this regime. For the case of T4B1, $T_c - T_m$ is negative when $\Delta T \geq 5$ K, which again suggests that the $\lambda = 4$ plate is more efficient

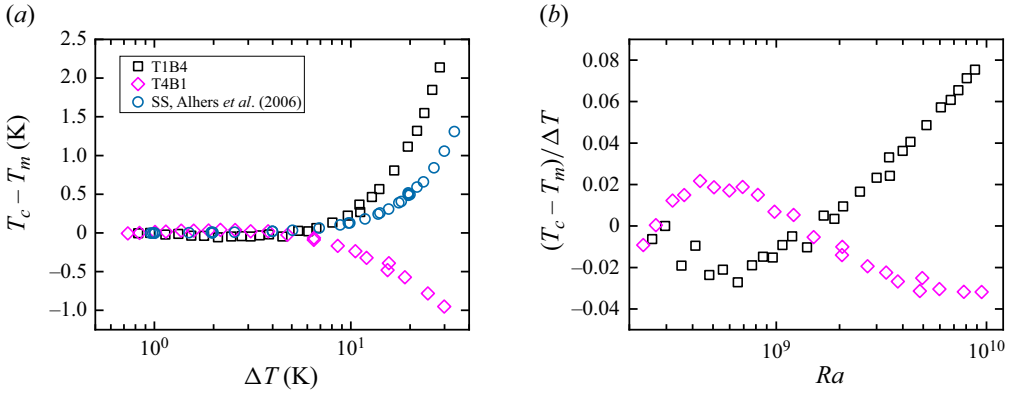

Figure 3. (*a*) The difference between the temperature T_c at the cell centre and the arithmetic mean temperature T_m of the conducting plates as a function of the applied temperature difference ΔT across the top and bottom plates. (*b*) The corresponding normalized temperature deviations as functions of the Rayleigh number. The legends are the same as those in panel (*a*).

in heat transfer than the $\lambda = 1$ plate. On the other hand, when the applied temperature difference is small ($\Delta T < 5\,\mathrm{K}$), for which the OB approximation is valid, the centre temperatures T_c show no apparent difference with T_m for all three cases. To have a clearer view of this regime, we plot in figure 3(*b*) the normalized centre temperature deviations $(T_c - T_m)/\Delta T$ as functions of the Rayleigh numbers for the two asymmetric cells. It is seen that for the low-Rayleigh-number regime ($Ra < Ra_c$), the signs of bulk temperature deviations are opposite to those measured in the high-Rayleigh-number regime for both the T1B4 and the T4B1 cases. This indicates that for $Ra < Ra_c$, the $\lambda = 1$ plate, in turn, shows a higher heat-transfer capability, regardless of whether it is assembled on the top or at the bottom.

We can now conclude that the heat-transfer capability of an individual plate is mainly determined by its topography and is not sensitive to the applied temperature boundary condition. For the two types of roughness explored in the present study with $\lambda = 1$ and 4, the former shows a higher heat-transfer efficiency (lower thermal impedance) at small Rayleigh numbers, whereas the latter dominates heat transport at high Rayleigh numbers. The critical Rayleigh number separating these two regimes is approximately $Ra_c = 1.9 \times 10^9$. At this particular Rayleigh number, the heat transport abilities of the two rough plates are balanced. It is also worth mentioning that the relative strength of heat transport abilities of individual plates deduced from centre temperature behaviours shows qualitative agreement with those measured in symmetric cells (see figure 2). In addition, we remark that when the bulk temperature T_c is higher (lower) than T_m, the temperature drop associated with the upper thermal boundary layer must be larger (smaller) than that of the lower thermal boundary layer. In this sense, the up–down symmetry of thermal boundary layers is very vulnerable to the change in boundary geometries.

Figure 4(*a*) shows the normalized centre temperature fluctuations $\sigma_{T_c}/\Delta T$ measured in asymmetric and symmetric rough cells, respectively. The same quantity measured in an SS cell is also plotted for reference (Wei *et al.* 2014). It is interesting to note that the centre temperature fluctuations, in general, show similar behaviours to the global heat transports (figure 2). The temperature fluctuations in symmetric/asymmetric rough cells are always larger than those measured in an SS cell. This agrees with the physical picture that roughness elements can trigger more plume-emission events and thus increase the intensity of turbulence. A transition is also discernible around $Ra = 1.9 \times 10^9$ for each rough data

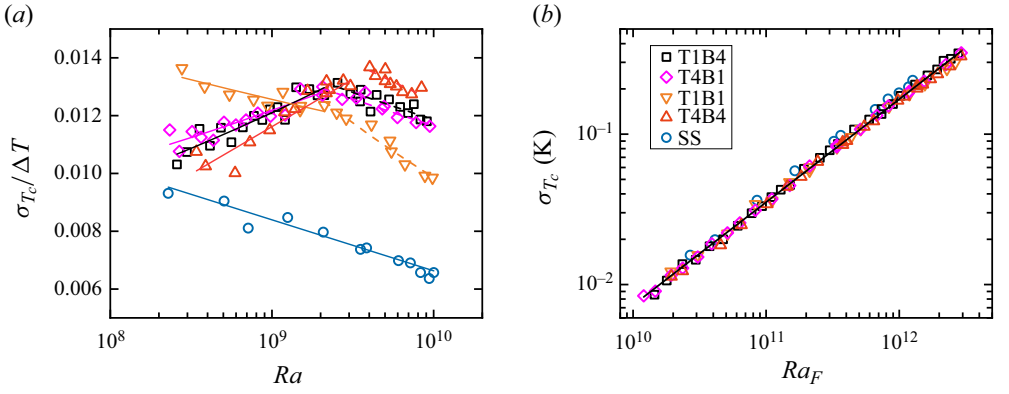

Figure 4. (*a*) The normalized bulk temperature fluctuations $\sigma_{T_c}/\Delta T$ as functions of Ra. The data for the SS case are adapted from Wei *et al.* (2014). The solid and dashed lines show power-law fits to the data. The fitting parameters are summarized in table 2. (*b*) The measured centre temperature fluctuations σ_{T_c} as functions of Ra_F. The solid line represents a power-law fit with $Ra_F^{0.68}$. Panels (*a*,*b*) share the same legend.

set. In addition, the curves for the two asymmetric rough cells collapse well onto each other, and they are both located in between the two curves representing symmetric rough cells. The solid and dashed lines in figure 4(*a*) indicate power-law fits of $\sigma_{T_c}/\Delta T = CRa^{\gamma}$ to the data before and after the transitional Rayleigh number, respectively. The fitting parameters are also summarized in table 2.

The fact that the centre temperature fluctuations (figure 4) and the global Nusselt numbers (figure 2) show a high degree of similarity indicates that they might be highly correlated. In figure 4(*b*), we plot the measured centre temperature fluctuation as a function of the flux Rayleigh number $Ra_F = NuRa$ (which is proportional to the total heat flux). Remarkably, all data sets collapse well onto a single master curve, regardless of whether the boundary is symmetric or asymmetric, rough or smooth. A single power-law fit to all the data points yields $\sigma_{T_c} \sim Ra_F^{0.68}$. In fact, by assuming $Nu \sim Ra^{\beta}$ and $\sigma_{T_c}/\Delta T \sim Ra^{\gamma}$, one can obtain $\Delta T \sim Ra \sim Ra_F^{1/(1+\beta)}$ and $\sigma_{T_c} \sim Ra_F^{(1+\gamma)/(1+\beta)}$. Therefore, the universal scaling observed in figure 4(*b*) implies $(1+\gamma)/(1+\beta) = 0.68 \approx 2/3$, or equivalently $\gamma \approx (2\beta - 1)/3$. The result above reveals that the centre temperature fluctuation is mainly determined by the total heat flux and is robust to the changes in the geometrical boundary conditions.

Next, we plot in figure 5(*a–c*) the probability density functions (p.d.f.s) of the centre temperature fluctuations measured at three different Rayleigh numbers ($Ra = 5.0 \times 10^8$, 2.0×10^9 and 5.0×10^9), which correspond to two heat-transfer regimes and the critical Rayleigh number (figure 2). It is quite remarkable that different combinations of individual rough plates show precisely the same p.d.f. at different Rayleigh numbers, and they all conform to an exponential distribution (see the solid lines in figure 5*a–c*), suggesting that thermal plumes are vigorous and turbulence is fully developed in the bulk region (Heslot, Castaing & Libchaber 1987). More importantly, the p.d.f.s in figure 5(*a–c*) are almost symmetric. To quantify this point, we plot in figure 5(*d*) the vertical profiles of the skewness coefficient S_T of the temperature fluctuation ($S_T = \langle (T_c - \langle T_c \rangle)^3 \rangle / \sigma_{T_c}^3$) measured at different Rayleigh numbers. We can see that the value of S_T is around zero in a region of $0.3 < z/H < 0.7$ for all cases. This is counterintuitive since, for most of the Rayleigh number range explored, the heat-transfer capabilities of the two asymmetric plates are not balanced, as discussed above. For example, when $Ra < Ra_c$, the thermal impedance of the top plate is lower than that of the bottom plate in a T1B4 asymmetric

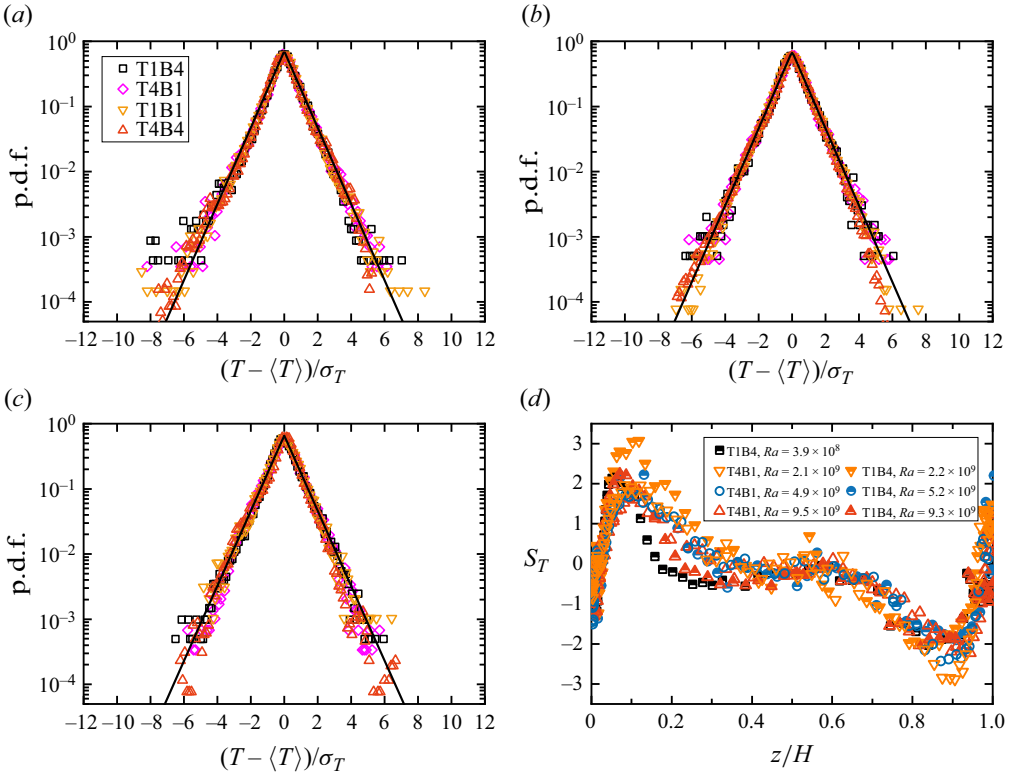

Figure 5. (*a–c*) Probability density functions (p.d.f.s) of the centre temperatures measured in different cells at $Ra = 5.0 \times 10^8$ (*a*), $Ra = 2.0 \times 10^9$ (*b*) and $Ra = 5.0 \times 10^9$ (*c*). The legends are the same as those in figure 4. The black lines show exponential distributions. (*d*) The vertical profiles of the temperature skewness measured in asymmetric rough cells at different Rayleigh numbers.

cell, so one might at first expect that the cold plumes emitted from the top plate are more intense than the hot plumes that come from the opposite plate. On the contrary, centre temperature measurements reveal that the symmetry of temperature fluctuation is robust to the symmetry breaking of boundary topography. In other words, for the bulk region of RBC with asymmetric geometrical boundaries, the symmetry of temperature fluctuation is spontaneously restored by adjusting the mean centre temperature T_c to a specific value. Such 'spontaneous symmetry restoring' behaviour can also be viewed as an inverse process of spontaneous symmetry breaking, which is often observed in condensed matter physics.

3.3. *Heat transport properties of individual rough plates*

With the centre temperature T_c, the Rayleigh number and Nusselt number of individual plates can be calculated as follows (Tisserand *et al.* 2011; Wei *et al.* 2014):

$$Ra_i = \frac{\alpha g\,(2\Delta T_i)\,H^3}{\nu\kappa}, \tag{3.1}$$

$$Nu_i = \frac{Q}{\chi\,(2\Delta T_i)\,/H}, \tag{3.2}$$

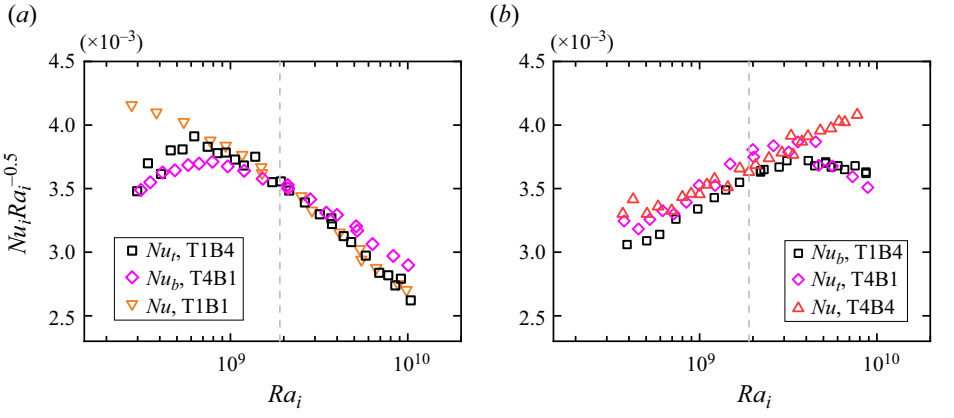

Figure 6. The Nu_i–Ra_i relations of (*a*) the $\lambda = 1$ rough plate and (*b*) the $\lambda = 4$ rough plate. The vertical dashed lines in both panels correspond to a transitional Rayleigh number of $Ra_c = 1.9 \times 10^9$.

where $\Delta T_i = |T_c - T_i|$, the subscript i represents the top plate ($i = t$) or the bottom plate ($i = b$), and χ is the thermal conductivity. Since the heat flux Q of the two plates is always balanced, when the centre temperature is higher than the arithmetic mean temperature of the two plates, i.e. $T_c > T_m$, we can readily obtain $\Delta T_t > \Delta T_b$, $Ra_t > Ra_b$ and $Nu_t < Nu_b$, which means that the bottom plate is better in heat transport than the top plate (and *vice versa*).

Figure 6(*a*,*b*) show the Nu_i–Ra_i relations of the $\lambda = 1$ plate and the $\lambda = 4$ plate calculated from various data sets. It is evident that for the low-Rayleigh-number regime ($Ra < Ra_c$), the heat-transfer efficiencies of the $\lambda = 1$ plate are higher than those of the $\lambda = 4$ plate, i.e. compensated values of $Nu_i Ra_i^{-0.5}$ for the $\lambda = 1$ plate are all larger than 3.5×10^{-3} and those of the $\lambda = 4$ plate are all smaller than 3.5×10^{-3}. Moreover, we also note from figure 6(*b*) that for this regime, the Nu_i–Ra_i relations of the $\lambda = 4$ plate measured in asymmetric and symmetric cells collapse with each other. But for the $\lambda = 1$ plate, the Nusselt numbers measured in asymmetric RB cells are apparently lower than in the symmetric case of T1B1. On the other hand, for the high-Rayleigh-number regime $Ra > Ra_c$, where the heat-transfer abilities of the $\lambda = 4$ plate dominate over those of the $\lambda = 1$ one, the curves of the $\lambda = 1$ plate in turn collapse (see figure 6*a*), while for the $\lambda = 4$ rough plate, Nusselt numbers measured in asymmetric cells show deviations from the symmetric case of T4B4. These observations suggest that the heat transport properties of individual rough plates can interact with each other in a 'one-way' manner. The Nusselt number of the plate with lower heat transport capability is robust, and it serves as a 'bottleneck' for the system's overall heat transfer. Meanwhile, this plate can considerably hinder the heat transport efficiency of the other plate with a higher heat-transfer efficiency. Such a 'one-way communication' interpretation is also applicable to a smooth–rough asymmetric turbulent RBC system (Tisserand *et al.* 2011; Wei *et al.* 2014), where the smooth plate always acts as the plate with lower heat-transfer ability.

3.4. *Bulk temperature inversion*

Figure 7 shows the vertical mean temperature profiles $(T(z) - T_c)/\Delta T$ measured at various Rayleigh numbers in the asymmetric rough cells. For the bulk region, all profiles collapse well with each other. A linear fit to all the data points in a range of $0.2 < z/H < 0.8$ yields $(T(z) - T_c)/\Delta T = 0.033 z/H - 0.016$. The positive slope of the

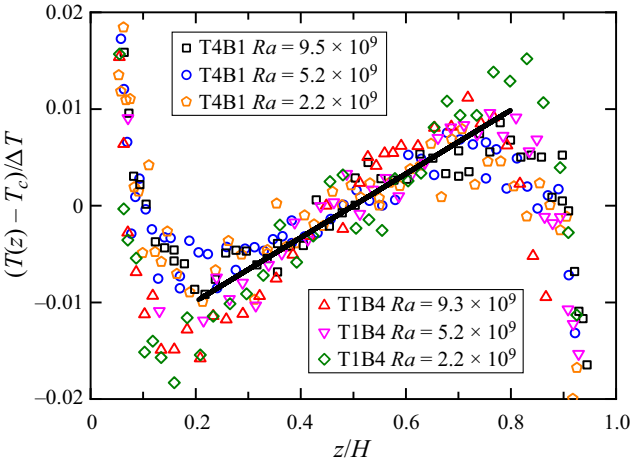

Figure 7. The normalized mean temperature profiles measured along the centre line of the asymmetric rough cells at different Rayleigh numbers. The black solid line shows a linear fit of $(T(z) - T_c)/\Delta T = 0.033z/H - 0.016$.

temperature profiles indicates that the flow is stably stratified in a time-averaged sense. A weak temperature inversion has also been reported in the bulk region of SS cells (Chillà *et al.* 1993; Tilgner, Belmonte & Libchaber 1993; Wang & Xia 2003; Maystrenko, Resagk & Thess 2007). However, we note that the non-dimensional temperature gradient obtained in the present asymmetric rough settings ($\partial T/\partial z = 0.033\Delta T/H$) is apparently stronger than those observed in SS cells. For example, Tilgner *et al.* (1993) obtained a value of $\partial T/\partial z = 0.019\Delta T/H$ at $Ra = 1.1 \times 10^9$ in a rectangular SS cell.

The bulk temperature inversion can be formed when the diffusion time scale of thermal plumes is much larger than the characteristic time scale of the LSC (Tilgner *et al.* 1993). In such a case, when the thermal plumes are emitted from one plate and then moved to the opposite side by the LSC, their enthalpies are not much dissipated and therefore can lead to a temperature inversion. Compared with smooth topography, a rough plate can significantly enhance the plume emission rate and promote the flow's coherency. For the present case, we believe that the thermalization time of the plume is also extended by the presence of both rough plates, resulting in a strong temperature inversion. Lastly, we remark that with the formation of a distinct stratification in a strong turbulent background, the present system might be a promising platform for studying the interplay between internal gravity waves and convection (Barel *et al.* 2020; He, Cheng & Xia 2022), which is an essential topic in physical oceanography and atmospheric turbulence.

3.5. *Reynolds numbers*

In this section, we explore the effects of asymmetric topographies on the Reynolds number associated with the LSC. It is known that the LSC undergoes ceaseless oscillations. The oscillation period τ_f of the LSC is determined by first calculating the autocorrelation function of the temperature time series measured by the thermistors embedded in the conducting plates, and then locating the position of the first peak (see figure 8*a*). For each case, the oscillation period of the LSC is averaged over all thermistors. With this, we can obtain the Reynolds number by $Re = 4H^2/(\tau_f \nu)$, where we have assumed $4H$ to be the typical length of the LSC flow path. It is worth mentioning that the above is only a first-order approximation since the exact length of the LSC flow path should be smaller

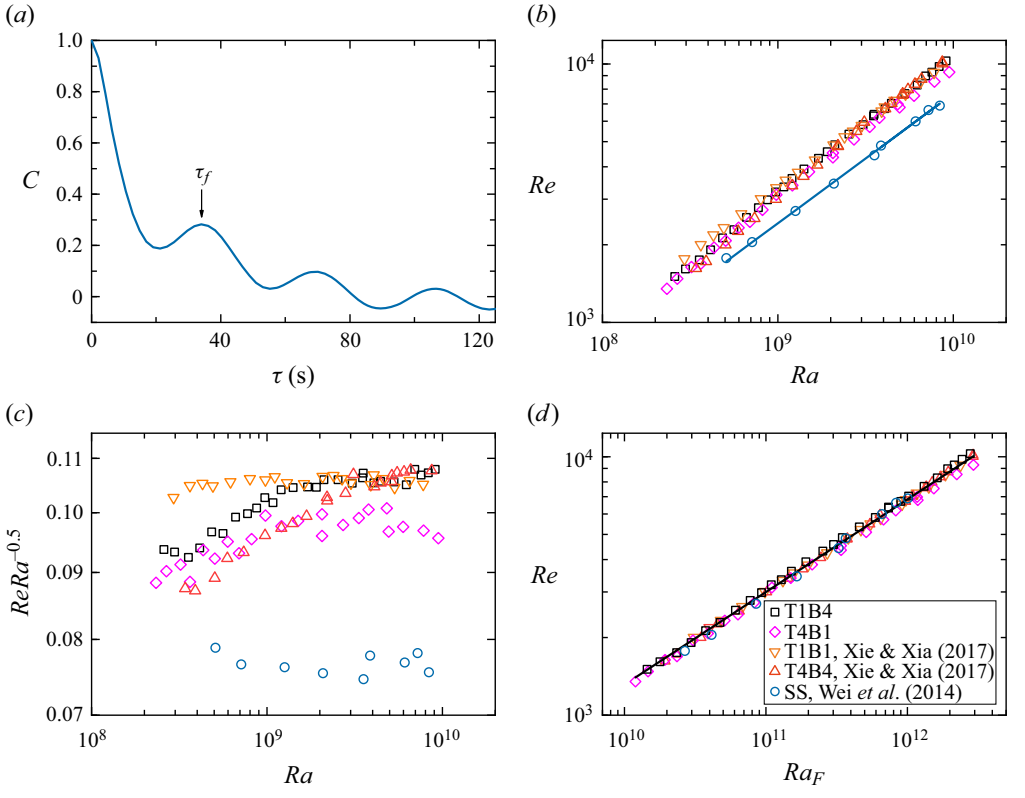

Figure 8. (*a*) An example of the autocorrelation function of the temperature time series. (*b*) The Reynolds number *Re* as functions of *Ra* for different sets of convection cells. (*c*) Compensated plots of $ReRa^{-0.5}$ versus *Ra*. (*d*) The Reynolds number as functions of the flux Rayleigh number Ra_F. The legends of panels (*b–d*) are the same.

than $4H$ and in general depends on the Rayleigh number (Niemela & Sreenivasan 2003; Sun & Xia 2005).

Figure 8(*b*) shows the *Re–Ra* relations measured in asymmetric and symmetric rough cells, respectively. The reference SS curve is adopted from Wei *et al.* (2014), which was obtained using the same method as in the present study. It is seen that the presence of rough plates results in a significantly higher *Re* than in the SS case. Compared with the Nusselt number behaviour (figure 2*a*), the Reynolds numbers for asymmetric and symmetric cells show a slighter deviation. For a clear view, we compensate *Re* with $Ra^{0.5}$ in figure 8(*c*). It is seen that the curve for a symmetric rough cell follows a power law, which is approximately $Re \sim Ra^{0.50}$ for T1B1 (downward triangles) and $Re \sim Ra^{0.57}$ for T4B4 (upward triangles). Similar to global heat transfer, the Reynolds number behaviours of the two asymmetric rough sets (T1B4 and T4B1) can also be divided into two regimes. For small Rayleigh numbers $Ra < Ra_c$, they are close to the T4B4 case. But in the large-Rayleigh-number regime $Ra \geq Ra_c$, their Reynolds numbers both show transitions to a power-law scaling around $Re \sim Ra^{0.5}$. The observation above is also consistent with the heat transport properties of individual plates (figure 6), i.e. when heat transport is dominated by the $\lambda = 1$ plate ($Ra < Ra_c$), the bottleneck of the $\lambda = 4$ plate lies in its capability of transporting not only heat but also momentum (and *vice versa* for $Ra \geq Ra_c$).

Lastly, we plot the Reynolds number *Re* as a function of the flux Rayleigh number Ra_F in figure 8(*d*). In this plot, all data points again collapse onto a single master curve of

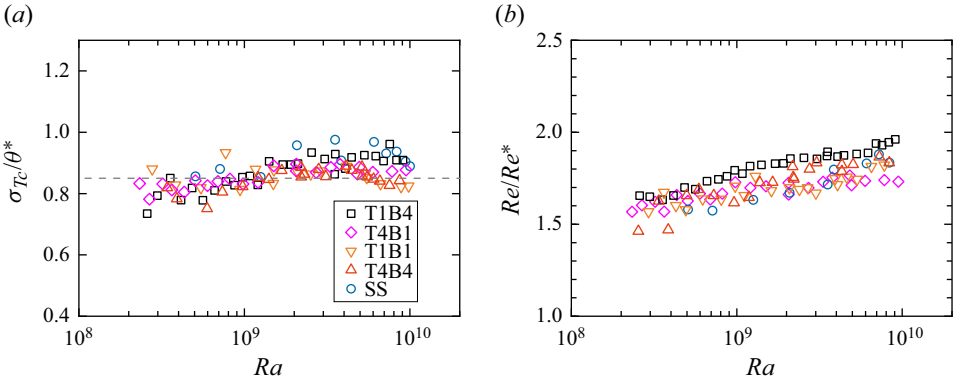

Figure 9. (*a*) The normalized centre temperature fluctuation σ_{Tc}/θ^* as a function of Ra. Here θ^* is the convective temperature scale. The horizontal dashed line shows $\sigma_{Tc}/\theta^* = 0.85$. (*b*) Plot of Re/Re^* as a function of Ra, where Re^* is defined by the convective velocity scale. The legends are the same as those in panel (*a*).

$Re = 0.34Ra_F^{0.36}$, as the temperature fluctuations do (figure 4*b*). This also suggests that the typical velocity of the LSC is also, to a large extent, determined by the overall heat flux Q that flows through the convection cell, regardless of whether the geometrical boundary is smooth or rough, symmetric or asymmetric.

3.6. *Convective temperature and velocity scales*

By dimensional analysis, Deardorff (1970) proposed that the convection temperature scale and convective velocity scale, which are expressed as $\theta^* \equiv Q^{2/3}/(\alpha g H)^{1/3}$ and $w_* \equiv (\alpha g H Q)^{1/3}$, can be used to describe the fluctuations of temperature and velocity in buoyancy-driven turbulence. More recently, Xie *et al.* (2019) reported that, when scaled with the convective temperature scale, the bulk temperature fluctuation in symmetric RBC remains constant ($\sigma_{T_c}/\theta^* = 0.85$) over a Rayleigh number range of $10^8 \leq Ra \leq 10^{15}$ and a Prandtl number range of $0.7 \leq Pr \leq 23.34$. In addition, the normalized vertical velocity fluctuation shows a weak positive Rayleigh number dependence.

For RBC with asymmetric topographies, we have shown that the positive and negative temperature fluctuations are symmetric (figure 5). So we can take the standard deviation of the centre temperature σ_T as the single typical scale of temperature fluctuation. Figure 9(*a*) presents the normalized centre temperature fluctuations σ_{Tc}/θ^* as functions of Rayleigh number measured in symmetric and asymmetric rough cells. It is seen that the curves for different cells approximately collapse onto each other, and the data points all fall around a value of 0.85 as reported by Xie *et al.* (2019). A single power-law fit to all the data yields a weak Rayleigh number dependence of $\sigma_{Tc}/\theta^* \sim Ra^{0.03}$. Similarly, we plot in figure 9(*b*) the ratio between the LSC-based Reynolds number Re and the Reynolds number defined by the convective velocity scale Re^*. The four rough cells with different symmetries again show the same trend, and a single power-law fit results in $Re/Re^* \sim Ra^{0.04}$. The analyses above suggest that, even when the boundary symmetric is broken, the convective scales (θ^* and w^*) are reasonable approximations of turbulent fluctuations in the bulk of the convection cell.

4. Conclusion

This paper reports the results of an experimental study on turbulent RBC with asymmetric geometric boundary topology realized by different roughness elements. The heat transport,

the temperature statistics in the bulk and the Reynolds number associated with the LSC are measured. It is found that the Nusselt number measured in the asymmetric rough cells is in between those of the symmetric rough cells, and they show good heat transport capability over a wide range of Rayleigh numbers when compared with the symmetric rough cases. The *Nu*–*Ra* behaviours of the asymmetric cells show two regimes: for $Ra < 1.9 \times 10^9$, the heat-transfer capability of the $\lambda = 1$ plate is greater than that of the $\lambda = 4$ plate; while for $Ra \geq 1.9 \times 10^9$, the $\lambda = 4$ plate, in turn, dominates the overall heat transport. Furthermore, in both regimes, the Nusselt number of the plate with higher heat-transfer ability will be reduced by the plate on the opposite side. In contrast, the Nusselt number of the plate with lower heat-transfer capability is unchanged.

The time-averaged centre temperature in an asymmetric rough cell can deviate from the mean temperature of the top and bottom plates even when the flow satisfies the OB approximation. This implies that the temperature drops associated with the top and bottom thermal boundary layers are not equal when the symmetry of boundary topology is broken. Counterintuitively, the symmetry of the centre temperature fluctuations is found to be robust even with asymmetric boundaries, evident from its p.d.f.s and skewness coefficients. When plotted against the flux Rayleigh number Ra_F, standard deviations of the centre temperature conform to a single power law of $\sigma_{T_c} \sim Ra_F^{0.68}$, regardless of whether the boundary is rough or smooth, symmetric or asymmetric. Measurements of the vertical temperature profiles reveal a temperature inversion in the bulk of symmetric/asymmetric rough cells, with a non-dimensionalized stratification of $\partial T/\partial z = 0.033\Delta T/H$, which is stronger than those reported in smooth cells. It is also shown that the convective temperature scale and velocity scale are appropriate scales in asymmetric RBC systems.

The asymmetry in boundary topography is also reflected in the Reynolds number *Re* associated with the LSC. It is found that the effective *Re*–*Ra* scaling changes across $Ra_c = 1.9 \times 10^9$. However, when *Re* is plotted against the flux Rayleigh number, a universal power law of $Re \sim Ra_F^{0.36}$ is observed.

To summarize, when different rough topologies break the up–down symmetry of RBC, turbulent convection evolves to a state in which the bulk temperature is closer to that of the plate with a higher heat-transfer efficiency. For heat transport efficiency, the interaction between the two plates can be generalized as a 'one-way communication'. Spontaneous symmetry restoration is observed in the sense of the centre temperature distribution, suggesting that turbulent fluctuations in the bulk are not sensitive to the symmetry properties of the boundaries. This conclusion also applies to the centre temperature fluctuation and the LSC Reynolds number, which both show universal power-law dependencies on the flux Rayleigh number. Thus, one can estimate the global heat transport by measuring the local fluctuations of the bulk flow, which may be very useful for natural systems when direct measurement of the global quantity is either technically inaccessible or impracticable owing to factors such as complex boundary topology or enormous system scale. The findings above may also help improve thermal design and thermal management in industrial applications, where roughness elements of different shapes are extensively involved.

Acknowledgements. We sincerely thank Mr J. Dong for his help with the experiments.

Funding. This work was supported by the National Natural Science Foundation of China (nos. 12072144, 92152104, 12232010 and 12202173) and the XJTU Young Talent Support Plan.

Declaration of interests. The authors report no conflict of interest.

Author ORCIDs.
Lu Zhang https://orcid.org/0000-0003-4009-2969;
Ke-Qing Xia https://orcid.org/0000-0001-5093-9014;
Yi-Chao Xie https://orcid.org/0000-0002-2159-4579.

References

Ahlers, G., Araujo, F.F., Funfschilling, D., Grossmann, S. & Lohse, D. 2007 Non-Oberbeck–Boussinesq effects in gaseous Rayleigh–Bénard convection. *Phys. Rev. Lett.* **98** (5), 054501.

Ahlers, G., Brown, E., Araujo, F.F., Funfschilling, D., Grossmann, S. & Lohse, D. 2006 Non-Oberbeck–Boussinesq effects in strongly turbulent Rayleigh–Bénard convection. *J. Fluid Mech.* **569**, 409–445.

Ahmed, H.E., Salman, B.H., Kherbeet, A.S. & Ahmed, M.I. 2018 Optimization of thermal design of heat sinks: a review. *Intl J. Heat Mass Transfer* **118**, 129–153.

Barel, L., Eidelman, A., Elperin, T., Fleurov, G., Kleeorin, N., Levy, A., Rogachevskii, I. & Shildkrot, O. 2020 Detection of standing internal gravity waves in experiments with convection over a wavy heated wall. *Phys. Fluids* **32** (9), 095105.

Belkadi, M., Guislain, L., Sergent, A., Podvin, B., Chillà, F. & Salort, J. 2020 Experimental and numerical shadowgraph in turbulent Rayleigh–Bénard convection with a rough boundary: investigation of plumes. *J. Fluid Mech.* **895**, A7.

Belkadi, M., Sergent, A., Fraigneau, Y. & Podvin, B. 2021 On the role of roughness valleys in turbulent Rayleigh–Bénard convection. *J. Fluid Mech.* **923**, A6.

Boussinesq, J. 1903 *Théorie Analytique de la Chaleur*, vol. 2. Gauthier-Villars.

Brown, E., Nikolaenko, A. & Ahlers, G. 2005 Reorientation of the large-scale circulation in turbulent Rayleigh–Bénard convection. *Phys. Rev. Lett.* **95** (8), 084503.

Chillà, F., Ciliberto, S., Innocenti, C. & Pampaloni, E. 1993 Boundary layer and scaling properties in turbulent thermal convection. *Il Nuovo Cimento* D **15** (9), 1229–1249.

Deardorff, J.W. 1970 Convective velocity and temperature scales for the unstable planetary boundary layer and for Rayleigh convection. *J. Atmos. Sci.* **27** (8), 1211–1213.

Demou, A.D. & Grigoriadis, D.G.E. 2019 Direct numerical simulations of Rayleigh–Bénard convection in water with non-Oberbeck–Boussinesq effects. *J. Fluid Mech.* **881**, 1073–1096.

He, Y.-H., Cheng, B.-Y.-C. & Xia, K.-Q. 2022 A laboratory study of internal gravity waves incident upon slopes with varying surface roughness. *J. Fluid Mech.* **942**, A26.

He, Z.-Q., Yan, Y.-F. & Zhang, Z.-E. 2021 Thermal management and temperature uniformity enhancement of electronic devices by micro heat sinks: a review. *Energy* **216**, 119223.

Heslot, F., Castaing, B. & Libchaber, A. 1987 Transitions to turbulence in helium gas. *Phys. Rev.* A **36**, 5870–5873.

Huang, S.-D., Wang, F., Xi, H.-D. & Xia, K.-Q. 2015 Comparative experimental study of fixed temperature and fixed heat flux boundary conditions in turbulent thermal convection. *Phys. Rev. Lett.* **115**, 154502.

Huang, H.L., Xu, W., Wang, Y., Wang, X.P., He, X.Z. & Tong, P. 2022 Fluctuation-induced slip of thermal boundary layers at a stable liquid–liquid interface. *J. Fluid Mech.* **951**, A10.

Jiang, H., Zhu, X., Mathai, V., Verzicco, R., Lohse, D. & Sun, C. 2018 Controlling heat transport and flow structures in thermal turbulence using ratchet surfaces. *Phys. Rev. Lett.* **120** (4), 044501.

Johnston, H. & Doering, C.R. 2009 Comparison of turbulent thermal convection between conditions of constant temperature and constant flux. *Phys. Rev. Lett.* **102** (6), 064501.

Krishnamurti, R. & Howard, L.N. 1981 Large-scale flow generation in turbulent convection. *Proc. Natl Acad. Sci. USA* **78** (4), 1981–1985.

Liot, O., Ehlinger, Q., Rusaouën, É., Coudarchet, T., Salort, J. & Chillà, F. 2017 Velocity fluctuations and boundary layer structure in a rough Rayleigh–Bénard cell filled with water. *Phys. Rev. Fluids* **2**, 044605.

Liot, O., Salort, J., Kaiser, R., Du Puits, R. & Chillà, F. 2016 Boundary layer structure in a rough Rayleigh–Bénard cell filled with air. *J. Fluid Mech.* **786**, 275–293.

Maystrenko, A., Resagk, C. & Thess, A. 2007 Structure of the thermal boundary layer for turbulent Rayleigh–Bénard convection of air in a long rectangular enclosure. *Phys. Rev.* E **75** (6), 066303.

Niemela, J.J. & Sreenivasan, K.R. 2003 Rayleigh-number evolution of large-scale coherent motion in turbulent convection. *Europhys. Lett.* **62** (6), 829.

Oberbeck, A. 1879 Über die Wärmeleitung der Flüssigkeiten bei Berücksichtigung der Strömungen infolge von Temperaturdifferenzen. *Ann. Phys. Chem.* **243** (6), 271–292.

VAN DER POEL, E.P., OSTILLA-MÓNICO, R., VERZICCO, R. & LOHSE, D. 2014 Effect of velocity boundary conditions on the heat transfer and flow topology in two-dimensional Rayleigh–Bénard convection. *Phys. Rev.* E **90** (1), 013017.

QIU, X.-L., XIA, K.-Q. & TONG, P. 2005 Experimental study of velocity boundary layer near a rough conducting surface in turbulent natural convection. *J. Turbul.* **6**, N30.

REN, L., TAO, X., ZHANG, L., NI, M.-J., XIA, K.-Q. & XIE, Y.-C. 2022 Flow states and heat transport in liquid metal convection. *J. Fluid Mech.* **951**, R2.

RUSAOUËN, E., LIOT, O., CASTAING, B., SALORT, J. & CHILLÀ, F. 2018 Thermal transfer in Rayleigh–Bénard cell with smooth or rough boundaries. *J. Fluid Mech.* **837**, 443–460.

SALORT, J., LIOT, O., RUSAOUEN, E., SEYCHELLES, F., TISSERAND, J.C., CREYSSELS, M., CASTAING, B. & CHILLÀ, F. 2014 Thermal boundary layer near roughnesses in turbulent Rayleigh–Bénard convection: flow structure and multistability. *Phys. Fluids* **26** (1), 015112.

SHEN, Y., TONG, P. & XIA, K.-Q. 1996 Turbulent convection over rough surfaces. *Phys. Rev. Lett.* **76** (6), 908–911.

STEVENS, R.J.A.M., LOHSE, D. & VERZICCO, R. 2011 Prandtl and Rayleigh number dependence of heat transport in high Rayleigh number thermal convection. *J. Fluid Mech.* **688**, 31–43.

SUN, C. & XIA, K.-Q. 2005 Scaling of the Reynolds number in turbulent thermal convection. *Phys. Rev.* E **72**, 067302.

SUN, C., XIA, K.-Q. & TONG, P. 2005 Three-dimensional flow structures and dynamics of turbulent thermal convection in a cylindrical cell. *Phys. Rev.* E **72** (2), 026302.

TILGNER, A., BELMONTE, A. & LIBCHABER, A. 1993 Temperature and velocity profiles of turbulent convection in water. *Phys. Rev.* E **47** (4), R2253.

TISSERAND, J.C., CREYSSELS, M., GASTEUIL, Y., PABIOU, H., GIBERT, M., CASTAING, B. & CHILLÀ, F. 2011 Comparison between rough and smooth plates within the same Rayleigh–Bénard cell. *Phys. Fluids* **23** (1), 015105.

TOPPALADODDI, S., WELLS, A.J., DOERING, C.R. & WETTLAUFER, J.S. 2021 Thermal convection over fractal surfaces. *J. Fluid Mech.* **907**, A12.

URBAN, P., KRALIK, T., MACEK, M., HANZELKA, P., VEZNIK, T. & SKRBEK, L. 2021 Effect of boundary conditions in turbulent thermal convection. *Europhys. Lett.* **134** (3), 34003.

VERZICCO, R. & SREENIVASAN, K.R. 2008 A comparison of turbulent thermal convection between conditions of constant temperature and constant heat flux. *J. Fluid Mech.* **595**, 203–219.

VIEWEG, P.P., SCHEEL, J.D. & SCHUMACHER, J. 2021 Supergranule aggregation for constant heat flux-driven turbulent convection. *Phys. Rev. Res.* **3** (1), 013231.

WAN, Z.-H., WANG, Q., WANG, B., XIA, S.-N., ZHOU, Q. & SUN, D.-J. 2020 On non-Oberbeck–Boussinesq effects in Rayleigh–Bénard convection of air for large temperature differences. *J. Fluid Mech.* **889**, A10.

WANG, J. & XIA, K.-Q. 2003 Spatial variations of the mean and statistical quantities in the thermal boundary layers of turbulent convection. *Eur. Phys. J.* B **32**, 127–136.

WEI, P., CHAN, T.-S., NI, R., ZHAO, X.-Z. & XIA, K.-Q. 2014 Heat transport properties of plates with smooth and rough surfaces in turbulent thermal convection. *J. Fluid Mech.* **740**, 28–46.

XI, H.-D., LAM, S. & XIA, K.-Q. 2004 From laminar plumes to organized flows: the onset of large-scale circulation in turbulent thermal convection. *J. Fluid Mech.* **503**, 47–56.

XI, H.-D. & XIA, K.-Q. 2007 Cessations and reversals of the large-scale circulation in turbulent thermal convection. *Phys. Rev.* E **75** (6), 066307.

XI, H.-D., ZHOU, S.-Q., ZHOU, Q., CHAN, T.-S. & XIA, K.-Q. 2009 Origin of the temperature oscillation in turbulent thermal convection. *Phys. Rev. Lett.* **102** (4), 044503.

XIE, Y.-C., CHENG, B.-Y.-C., HU, Y.-B. & XIA, K.-Q. 2019 Universal fluctuations in the bulk of Rayleigh–Bénard turbulence. *J. Fluid Mech.* **878**, R1.

XIE, Y.-C., WEI, P. & XIA, K.-Q. 2013 Dynamics of the large-scale circulation in high-Prandtl-number turbulent thermal convection. *J. Fluid Mech.* **717**, 322–346.

XIE, Y.-C. & XIA, K.-Q. 2013 Dynamics and flow coupling in two-layer turbulent thermal convection. *J. Fluid Mech.* **728**, R1.

XIE, Y.-C. & XIA, K.-Q. 2017 Turbulent thermal convection over rough plates with varying roughness geometries. *J. Fluid Mech.* **825**, 573–599.

ZHANG, L., DING, G.-Y. & XIA, K.-Q. 2021 On the effective horizontal buoyancy in turbulent thermal convection generated by cell tilting. *J. Fluid Mech.* **914**, A15.

ZHOU, Q., XI, H.-D., ZHOU, S.-Q., SUN, C. & XIA, K.-Q. 2009 Oscillations of the large-scale circulation in turbulent Rayleigh–Bénard convection: the sloshing mode and its relationship with the torsional mode. *J. Fluid Mech.* **630**, 367–390.

ZHU, X.-J., STEVENS, R.J.A.M., SHISHKINA, O., VERZICCO, R. & LOHSE, D. 2019 $Nu \sim Ra^{1/2}$ scaling enabled by multiscale wall roughness in Rayleigh–Bénard turbulence. *J. Fluid Mech.* **869**, R4.